Oxidation behavior at 1000°C of low–Mn high–Cr {Cantor's HEA}–based alloys strengthened or not by MC carbides

Pauline Spaeter , Corentin Gay , Nassima Chenikha , Ghouti Medjahdi , Anne Vernière , Christophe Rapin , Lionel Aranda , Patrice Berthod *

Posted Date: 19 July 2023

doi: 10.20944/preprints202307.1329.v1

Keywords: Modified Cantor alloys; Manganese; Chromium; TaC; HfC; High temperature oxidation

Article

Oxidation behavior at 1000°C of Low–Mn High–Cr {Cantor's HEA}–Based Alloys Strengthened or Not by MC Carbides

Pauline Spaeter [1], Corentin Gay [1], Nassima Chenikha [1], Ghouti Medjahdi [2], Anne Vernière [3], Christophe Rapin [3], Lionel Aranda [3] and Patrice Berthod [3,*]

[1] Faculté des Sciences et Technologies, Université de Lorraine, 54000 Vandoeuvre–lès-Nancy, France; pauline.spaeter8@etu.univ-lorraine.fr; corentin.gay8@etu.univ-lorraine.fr; nassima.chenikha5@etu.univ-lorraine.fr
[2] CC X-Gamma, Institut Jean Lamour, Université de Lorraine, 54000 Nancy, France; ghouti.medjahdi@univ-lorraine.fr
[3] CNRS, Institut Jean Lamour, Université de Lorraine, 54000 Nancy, France; anne.verniere@univ-lorraine.fr; christophe.rapin@univ-lorraine.fr; lionel.aranda@univ-lorraine.fr
* Correspondence: patrice.berthod@univ-lorraine.fr; Tel.: +33-3-72-74-27-29

Abstract: A conventionally cast CoNiFeMn0.5Cr1.5 alloy and two versions with 0.25C&3.7Ta or 0.25C&3.7Hf were tested in oxidation at 1000°C for 50h with thermogravimetric recording of the oxidation kinetic. In all cases the obtained mass gain curves are parabolic. Their parabolic constants are much lower than the Kp previously determined for the original alloys with an equimolar base (CoNiFeMnCr). However, the post–mortem exploitation of the oxidized samples revealed analogous oxidation features on surface and subsurface, with here too external oxide strata on surface with different Mn and Cr contents, and rather great Mn–depletion in addition to a moderate Cr–depletion, in subsurface. Globally, the oxidation behavior is significantly better than earlier observed for the equimolar version of these alloys.

Keywords: Modified Cantor alloys; Manganese; Chromium; TaC; HfC; High temperature oxidation

1. Introduction

Superalloys, the metallic alloys with outstanding high temperature properties in the fields of mechanical behavior and corrosion resistance [1], are the most often based on elements which are more and more considered as critical: namely nickel and cobalt [2]. The recent appearance of the high entropy compositions allows expecting moderate replacement of Ni and Co by cheaper and more abundant elements without dramatic losses of properties and even, contrariwise, with possible increase of these ones. Among the high entropy alloys (HEAs) the chemical compositions of which stay rather close to the superalloys bases, there is the {Co, Ni, Fe, Mn, Cr} quinary system [3-5]. In this system, the presence of the five elements in equal atomic quantities [6-8], known as the Cantor's composition, is certainly the best known. Although that this equimolar quinary alloy was not really considered as a possible base for high temperature applications first attempts of reinforcement by refractory carbides of the MC–type were undertaken [9–10] and led to promising creep resistance potential [11]. Unfortunately, it also appeared that these new alloys presented serious problems of oxidation. The detrimental role of manganese and the deleterious effect of a too low content in chromium were pointed out [12].

These two elements are of interest in the present work which explores the consequences, on the oxidation behavior of these alloys at 1000°C, of a 50% reduction of the manganese content simultaneously to a 50% augmentation of the chromium content. Because of these changes, the new alloys investigated in this work are more to be considered as Medium Entropy Alloys (MEAs) than as High Entropy Alloys (HEAs). For this reason they will be thereafter named "MEA/TaC" for the {3.7Ta,0.25C, wt.%}–added version, "MEA/HfC" for the {3.7Hf,0.25C, wt.%}–added version, and simply "MEA" for the carbide–free $CoNiFeMn_{0.5}Cr_{1.5}$ reference alloy.

2. Materials and Methods

Preprints (www.preprints.org) | NOT PEER-REVIEWED | Posted: 19 July 2023 doi:10.20944/preprints202307.1329.v1

2.1. Characteristics of the Alloys Available for This Study

In fact, these three alloys derived from the CoNiFeMnCr HEA alloys reinforced by either TaC [9] or HfC [10] were recently cast and their as–cast microstructures characterized [13]. Despite their modified chemical compositions (reminded in Table 1) from the equimolar original alloys [8,9], it was observed that the microstructures of the just solidified $CoNiFeMn_{0.5}Cr_{1.5}$–TaC (MEA/TaC) or –HfC (MEA/HfC) alloys stayed unchanged. This can be checked in the illustrations displayed in Figure 1.

Table 1. Chemical compositions of the three alloys (determined from five ×250 full frame EDS analyses per alloy); weight contents in all elements except carbon (for C: 0.25wt.% for the MEA/TaC and MEA/HfC alloys).

MEA Full frame (wt.%)	Co	Ni	Fe	Mn	Cr	M
Average	20.0	20.5	19.8	8.3	31.3	/
Standard deviation	0.1	0.3	0.18	0.5	0.4	/
MEA/TaC Full frame (wt.%)	**Co**	**Ni**	**Fe**	**Mn**	**Cr**	**Ta**
Average	19.5	20.0	19.1	8.4	28.5	4.6
Standard deviation	0.2	0.5	0.3	0.2	0.3	0.2
MEA/HfC Full frame (wt.%)	**Co**	**Ni**	**Fe**	**Mn**	**Cr**	**Hf**
Average	19.7	20.1	19.1	8.8	27.8	4.5
Standard deviation	0.4	0.3	0.3	0.3	0.7	0.6

Recent X-ray diffraction runs and electron microscopy observations [13] demonstrated that MEA alloy is still single–phased (FCC), the MEA/TaC double–phased (FCC matrix + interdendritic eutectic script–like TaC) and the MEA/HfC double–phased too (FCC matrix + HfC carbides). In the later alloy the HfC carbides are again present with two distributions and shapes: clusters of some pre–eutectic compact carbides (minor part) and interdendritic eutectic script–like carbides (major part). Higher magnification electron micrographs are provided in Figure 2 and allow better distinguishing the script – like shapes of the eutectic TaC and HfC carbides present in the interdendritic and intergranular spaces.

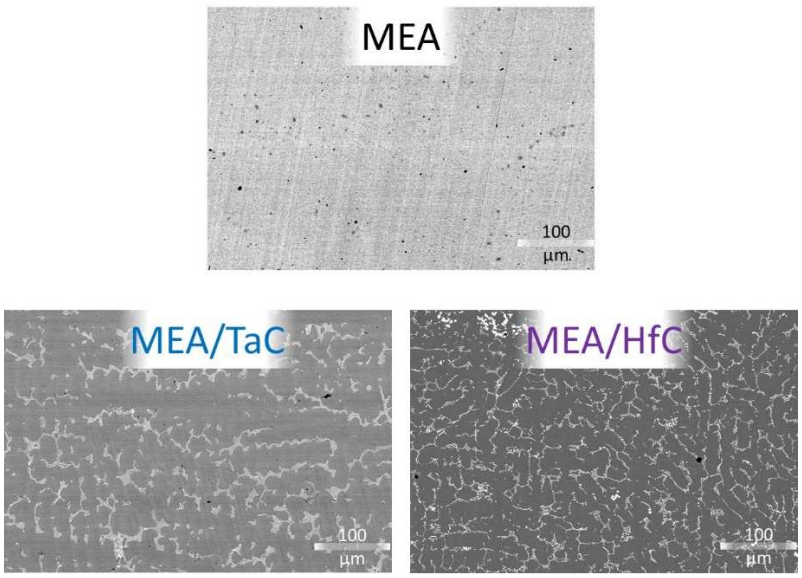

Preprints (www.preprints.org) | NOT PEER-REVIEWED | Posted: 19 July 2023 doi:10.20944/preprints202307.1329.v1

Figure 1. As–cast microstructures of the three as–cast CoNiFeMn$_{0.5}$Cr$_{1.5}$–based alloys (electron microscopy images taken in back scattered electrons mode).

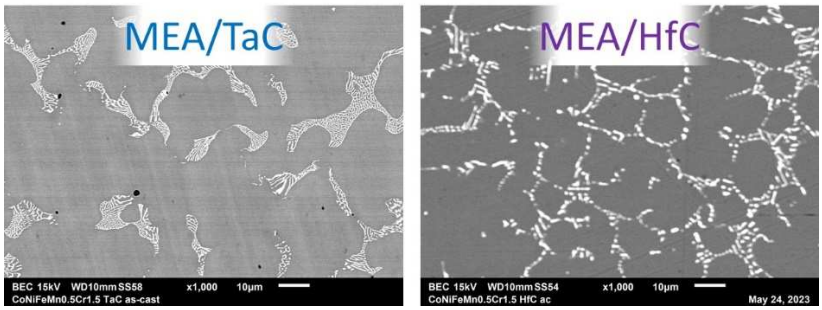

Figure 2. As–cast microstructures of the two MC–containing CoNiFeMn$_{0.5}$Cr$_{1.5}$–based alloys (electron microscopy images taken in back scattered electrons mode).

2.2. Oxidation Tests and Exploitation

Parallelepiped samples, with 10 mm × 10 mm × 2 mm as approximate dimensions were cut in the remaining parts of the ingots elaborated in [13], and ground all around with #1200–grit SiC papers. Special attention was given to edges and corners which were softened with the same papers, to prevent against possible local over–oxidation.

The oxidation tests were carried out in a synthetic air flow (dry 80%N_2–20%O_2, Alphagaz 1), with thermogravimetric follow–up of the oxidation progress. The used thermobalance was a SETARAM TGA 92-16.18 one. The applied thermal cycle was composed of a 20K min^{-1}–heating, a 50 hours–isothermal stage at 1,000°C, and a -5K min^{-1}–cooling.

The oxidized samples were subjected to X–Ray Diffraction (XRD) using a BRUKER D8 Advance spectrometer, working with a copper source (Kα, λ = 1.5406 Å). They were thereafter embedded in resin (XF40) + hardener (XH40) from NX MET. Each embedded sample was cut using a metallographic saw in two equal parts which were ground (SiC papers from #240–grit to #1200–grit) and polished (1 µm hard particles). The obtained cross–sectional mirror–like metallographic samples were observed with a Scanning Electron Microscope (SEM) from JEOL (JSM 6010–LA model), mainly in Back Scattered Electrons (BSE) mode and under a 20kV acceleration voltage. The external and internal oxides were imaged and analyzed with spot analyses carried out using the Energy Dispersion Spectrometer (EDS) attached to the SEM. Concentration profiles were acquired in the subsurface perpendicularly to the oxide {scale/alloy} interface. Elemental EDS cartography was also performed to better observe the distribution of the metallic elements in oxides and in alloy over the zone affected by oxidation.

3. Results

3.1. Thermogravimetry

The mass gain curve obtained for the MEA alloy, plotted versus time and plotted versus the square root of time are presented in Figure 3. The same are given for the MEA/TaC alloy in Figure 4 and for the MEA/HfC alloy in Figure 5.

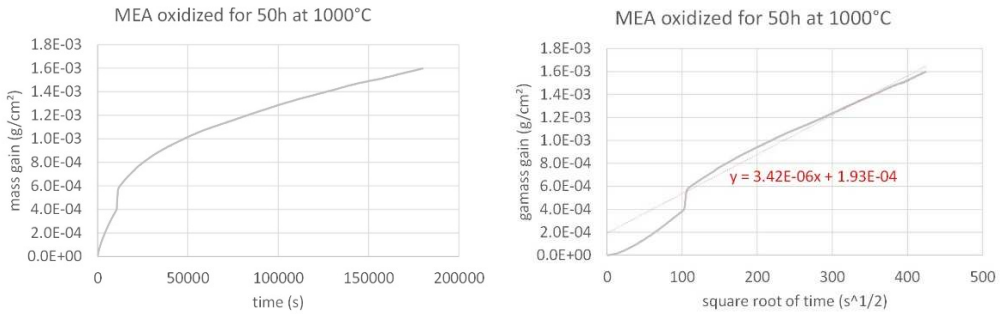

Figure 3. Isothermal mass gain kinetic of the MEA alloy at 1,000°C (left: versus time, right: versus the square root of time).

Preprints (www.preprints.org) | NOT PEER-REVIEWED | Posted: 19 July 2023 doi:10.20944/preprints202307.1329.v1

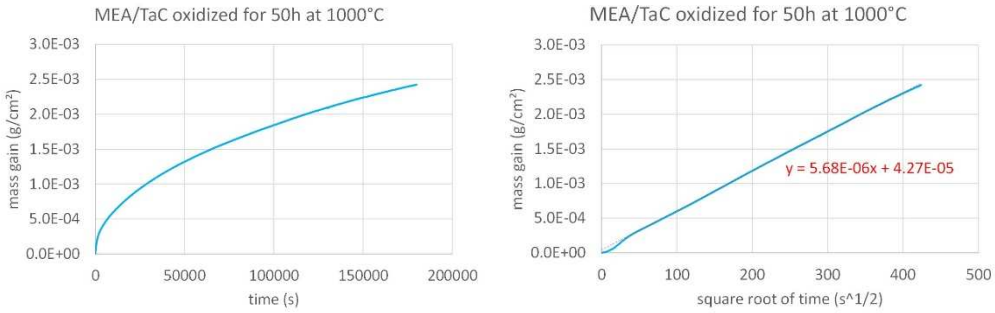

Figure 4. Isothermal mass gain kinetic of the MEA/TaC alloy at 1,000°C (left: versus time, right: versus the square root of time).

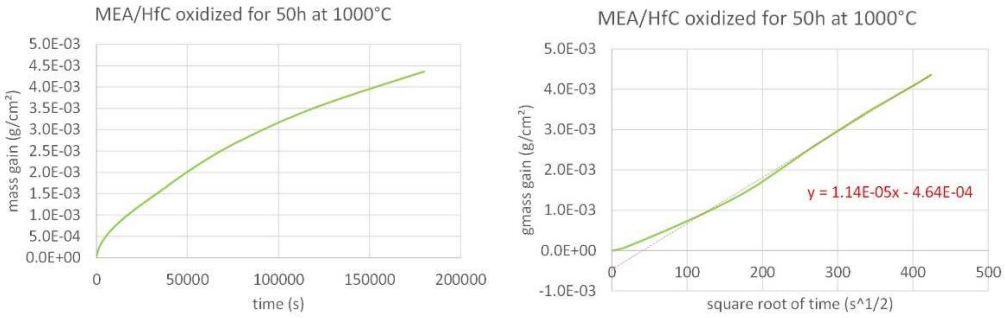

Figure 5. Isothermal mass gain kinetic of the MEA/HfC alloy at 1,000°C (left: versus time, right: versus the square root of time).

The three mass gain curves plotted versus time seems parabolic, which strongly suggests that a continuous external oxide scale developed all around the samples and isolated the alloy from hot air at the early beginning of the isothermal stage. One must just notice the presence of a small jump in the MEA's one which can be easily attributed to a local unsticking of the externally growing oxide scale, quickly healed. Thus, it appears obvious that the isothermal oxidation obeys the Wagner's law, without apparent linear oxidation nor linear oxide evaporation. This led to plot them versus the square root of time in order to estimate the corresponding parabolic constants (Kp). In this second representation mode a tenuous linear mass loss – superposed to the parabolic mass gain – seems existing for the MEA alloy (last half of the curve slightly concave) while a linear mass gain - tenuous too, superposed to the parabolic regime – can be suspected for the MEA/HfC alloy (last half of the curve slightly convex). Despite these observations, it was decided to access to a valuable estimation of the parabolic constants, from the slope of the regression straight lines drawn in the {mass gain versus square root of time} representations. The results are given in Table 2.

Table 2. Chemical compositions of the three alloys (determined from five ×250 full frame EDS analyses per alloy); weight contents in all elements except carbon (for C: 0.25wt.% for the MEA/TaC and MEA/HfC alloys)

Kp	Carbide–free alloy	TaC–containing alloy	HfC–containing alloy
$\times 10^{12}$ $g^2\ cm^{-4}\ s^{-1}$	**6**	**16**	**65**

3.2. Surface Analysis Prior to Cutting

Before the cross–sectional metallographic preparation for phase's imagining and chemical analysis, the oxidized samples were exposed to Cu Kα radiations for XRD analysis. The obtained diffractograms are displayed in Figure 6 for the MEA alloy, in Figure 7 for the MEA/TaC alloy and in Figure 8 for the MEA/HfC alloy.

Preprints (www.preprints.org) | NOT PEER-REVIEWED | Posted: 19 July 2023 doi:10.20944/preprints202307.1329.v1

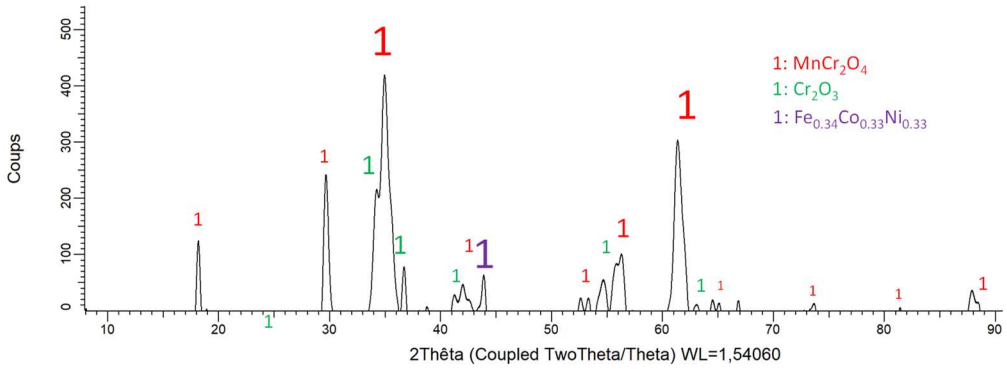

Figure 6. Diffractogram resulting of the XRD analysis of the oxidized surface of the MEA alloy.

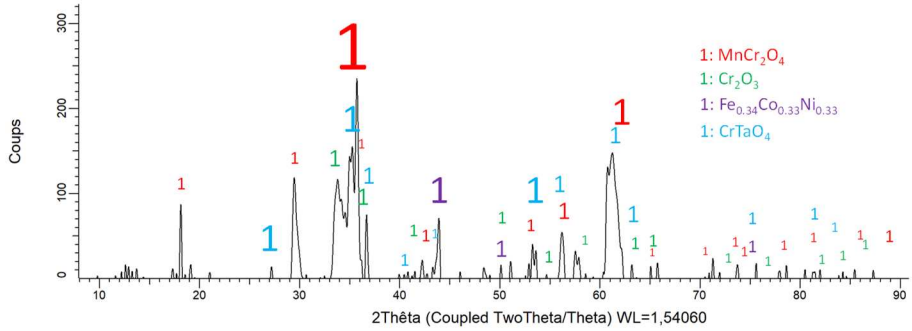

Figure 7. Diffractogram resulting of the XRD analysis of the oxidized surface of the MEA/TaC alloy.

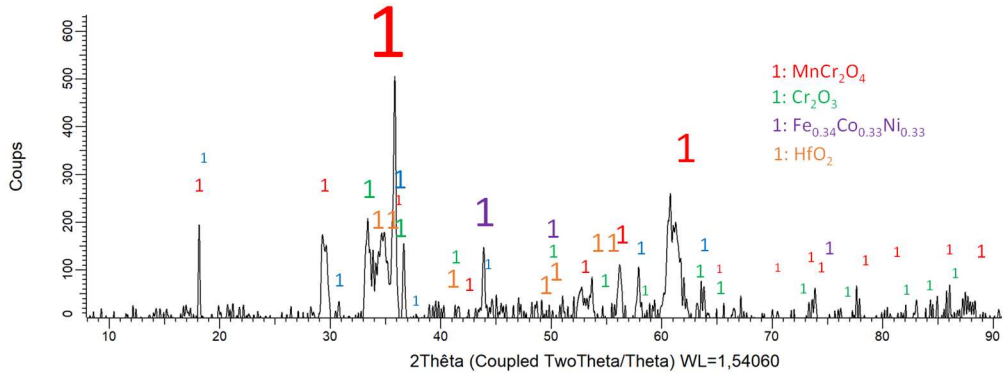

Figure 8. Diffractogram resulting of the XRD analysis of the oxidized surface of the MEA/HfC alloy.

Because of a more or less extended oxide spallation occurred during the cooling, the matrix is detected by XRD for the three alloys. The other peaks can be attributed to the formed oxides. Obviously this is the $MnCr_2O_4$ spinel which takes part to the three diffraction patterns. Chromia (Cr_2O_3) is present in all cases too, but with much lower intensities. Other oxides seems to be present, albeit with low peak heights too, $CrTaO_4$ for the MEA/TaC alloy, and HfO_2 for the MEA/HfC alloy.

3.3. Metallography in Cross–Section

Figure 9 illustrates the oxidation products and indirect effects with a low magnification and high magnification SEM/BSE micrographs. First, the oxide scales formed externally have obviously suffered from spallation during cooling. Second, no internal oxidation occurred in the subsurface of the MEA alloy while, for the MEA/TaC alloy, several particles of $CrTaO_4$ oxide appeared on the oxidation front (oxide scale/alloy interface) and in the subsurface region close to the oxidation front. At the same time a TaC–free zone developed from the scale/alloy interface. Subsurface oxidation features are different for the MEA/HfC alloy since oxidation seems penetrating inwards the alloy in addition to the external oxidation. Elemental cartography of these zones was realized for the three

Preprints (www.preprints.org) | NOT PEER-REVIEWED | Posted: 19 July 2023 doi:10.20944/preprints202307.1329.v1

alloys and the corresponding X–maps are displayed in Figure 10, Figure 11 and Figure 12 for the MEA alloy, MEA/TaC alloy and MEA/HfC alloys, respectively.

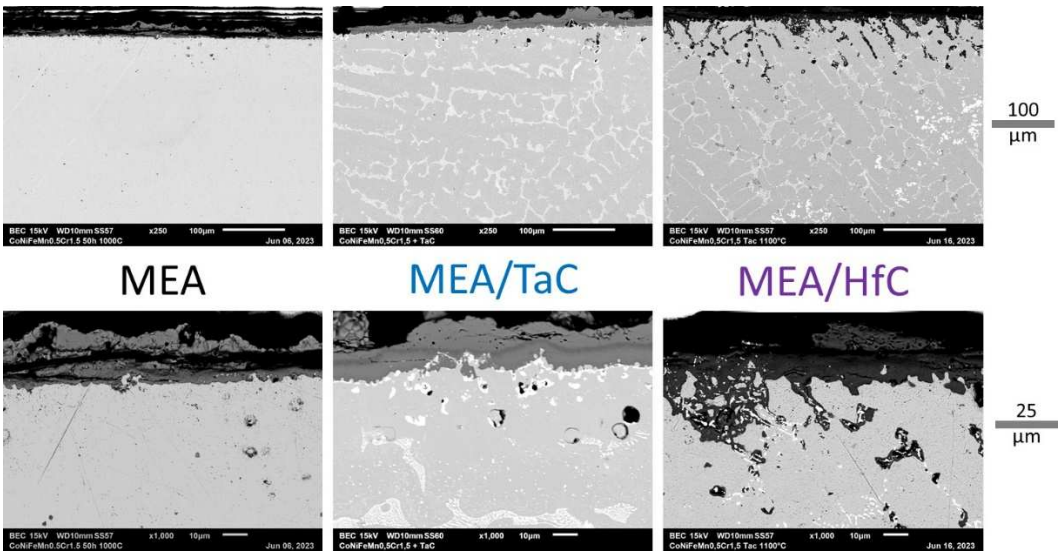

Figure 9. Cross–sectional imaging of the oxide scales and oxidation–affected subsurfaces.

The X–maps corresponding to the oxidized MEA alloy (Figure 10) clearly show a particular structure of the external scale, with an outer part much richer in Mn than in Cr and an inner one especially rich in Cr. Fe seems also being a little present with Mn in the outer part. In the subsurface one can observe the impoverishment in Mn, and also in Cr over a lower depth. In contrast, Co, Ni and even Fe seem to stay homogeneous in the subsurface, which is logical since they do not take part to the oxide formation. Concerning the MEA/TaC alloy (Figure 11), which lost its external scale in the location where the X–map was acquired, the elemental EDS cards well show the TaC carbides, as well as the subsurface impoverishment in Mn and in C, and, again, the still homogeneous repartition of Co, Ni and Fe, seemingly not influenced by the oxidation taking place nearby.

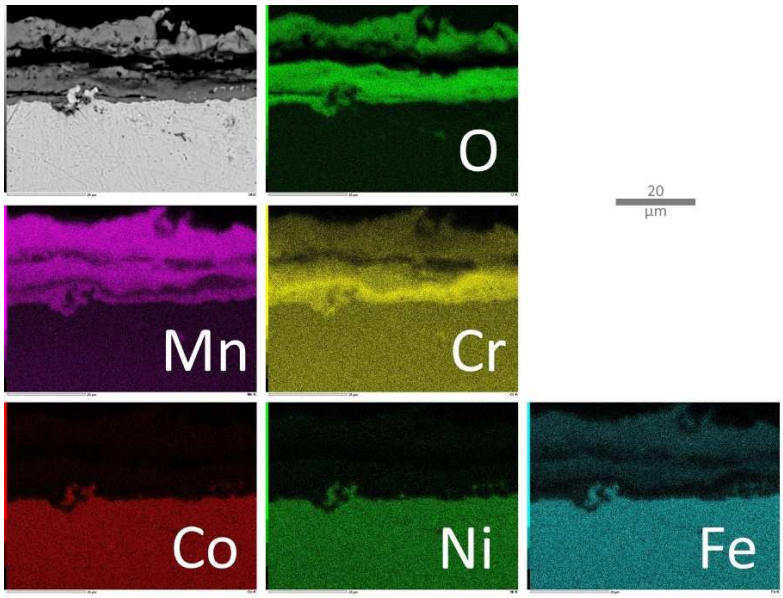

Figure 10. Elemental EDS cartography acquired on the oxide scale and the part of subsurface modified by oxidation in the case of the MEA alloy.

Preprints (www.preprints.org) | NOT PEER-REVIEWED | Posted: 19 July 2023 doi:10.20944/preprints202307.1329.v1

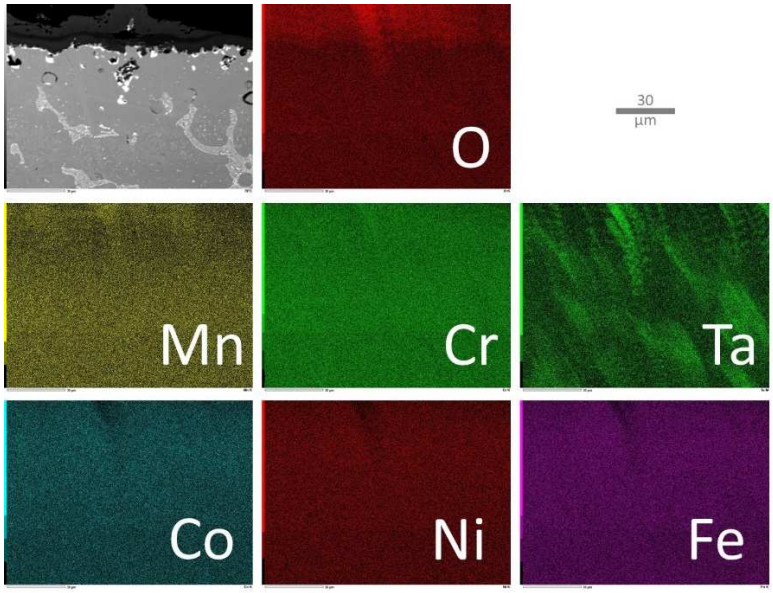

Figure 11. Elemental EDS cartography acquired on the oxide scale and the part of subsurface modified by oxidation in the case of the MEA/TaC alloy.

In the case of the MEA/HfC alloy (Figure 12), the same configuration of the external oxide scale concerning manganese and chromium is found again. In addition, X – mapping evidences the internal oxidation of Mn and Cr, as well as the in situ oxidation of the HfC carbides next to the oxidation front, with the progressive conversion of carbide into oxide (visible when comparing the O and Hf maps). The consequences on the Mn and Cr diffusion towards the oxidation front, the gradients of the concentrations of these elements, are also clearly evidenced. Again, the distributions of Co, Ni and Fe are homogeneous.

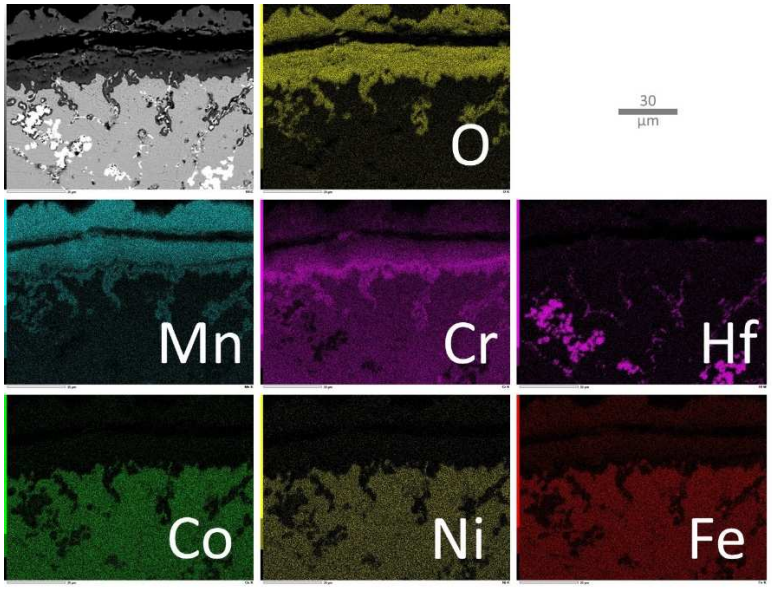

Figure 12. Elemental EDS cartography acquired on the oxide scale and the part of subsurface modified by oxidation in the case of the MEA/HfC alloy.

The progressive empoverishment in Mn and Cr when going closer and closer to the oxidation front is more quantatively revealed by EDS profiles acquired perpendicularly to the front (Figure 13). The decrease in both elements led to very low contents values next to the interface with the external surface, which are mentionned in Table 3.

Table 3. Minimal Cr and Mn contents close to the oxidation front and the corresponding impoverished depths.

Preprints (www.preprints.org) | NOT PEER-REVIEWED | Posted: 19 July 2023 doi:10.20944/preprints202307.1329.v1

Alloy		Cr mini (wt.%)	Cr–depleted depth (µm)	Mn mini (wt.%)	Mn–depleted depth (µm)
MEA	Max	25.1	62	3.4	93
	min	22.0	45	0.7	47
MEA/TaC	Max	20.3	59	1.2	122
	min	18.0	46	0.8	104
MEA/HfC	Max	21.63	95	1.39	175
	min	21.00	61	0.96	107

The lowest values of Cr contents close to the oxidation front are observed for the two carbides–containing alloys, with about 21 wt.%Cr against 25wt.%Cr for the quinary alloy. The same hierarchy exists concerning the minmal Mn content (1 to 1.5 wt.%Mn for the MEA/TaC and MEA/HfC alloys, against more than 3wt.%Mn for the MEA one). About the Cr and Mn impoverisment depths, there are no significant difference between the MEA and the MEA/TaC alloys. In contrast, the Cr and Mn depleted zones extend deeper for the MEA/HfC alloy.

4. Discussion

Thus, having first checked that the chemical composition changes tested here had no visible consequences on the microstructure (notably on the characteristics of the reinforcing MC carbides network), it was a good surprise (but expected) to observe that the oxidation behavior at 1,000°C was significantly improved by comparison to the equimolar base versions of these alloys. This was essentially demonstrated by the parabolic kinetics which are much slower than the ones of the {equimolar CoNiFeMnCr}–based alloys previously tested [14]: 6, 16 and 65 $\times 10^{-12}$ g^2 cm^{-4} s^{-1} for the MEA, MEA/TaC and MEA/HfC present alloys, against 60, 75 and 162 $\times 10^{-12}$ g^2 cm^{-4} s^{-1} for their corresponding equimolar versions respectively. Second, if the minimal Mn contents close to the oxidation front are almost the same as the equimolar version, the minimal Cr contents are still above 20 wt.% (i.e. the content allowing classical superalloys to stay longer chromia–forming) while the minimal Cr contents of the equimolar versions were lower than 10 wt.% and even 5 wt.%. However, the values of parabolic constants of the present $CoNiFeMn_{0.5}Cr_{1.5}$–based alloys are higher than the one of chromia–forming alloys as the binary Ni–30wt.%Cr at the same temperature ($< 3 \times 10^{-12}$ g^2 cm^{-4} s^{-1}) [15]. Further, the oxide scale structure is complex (sandwich type with an outer Mn–rich oxide and an inner Cr–rich one) and consequently not resistant enough to growth compression stresses and/or to shear stresses induce by differential thermal contraction. In contrast with the compact and adherent chromia oxide scales developed on the Ni–30wt.%Cr alloy and on many other chromia–forming alloys and superalloys, the oxide scales developed over the present modified Cantor's alloys are not compact nor tough and they too easily know spallation. Manganese, which demonstrated its high usefulness for promoting high mechanical properties at normal and low temperature, is here – in contrast – deleterious for the oxidation behavior at high temperature, by its intervention in the oxide scales that its involvement for promoting mixed oxides at the expense of chromia which is much less present as in Mn–free or Mn–poor alloys with the sale content in chromium. This detrimental effect is furthermore helped by its seemingly easier diffusion than for chromium, as suggested by the Mn–depleted subsurface zones deeper than the Cr–depleted ones.

5. Conclusions

So, decreasing the presence of Mn and increasing the Cr one have obviously very positive influence on the behavior in oxidation at high temperature of the Cantor's alloy and its derived versions strengthened by MC carbides. However, the oxidation kinetics are still faster than the really chromia–forming alloys and the oxides scales, heterogeneous in oxide nature and presenting multiple defects (including shear cracks), suggest catastrophic behavior in the thermal cycling conditions which are commonly met in service for high temperature industrial components. New decrease in Mn is to be envisaged, maybe down to close to 2 or 1 wt.%, values which may induce positive effects (such as lowering the volatilization of chromia at T > 1000°C). With so low Mn content the quinary

MEA base should become a quaternary base which is not longer a MEA or HEA alloy. Another solution can be replacing Mn by another element. Cu can be a candidate, as well as Al, which is otherwise, as Cr, useful to combat hot oxidation. Further work will soon deal with such substitution tests.

Author Contributions: For research articles with several authors, a short paragraph specifying their individual contributions must be provided. The following statements should be used "Conceptualization, P.B.; methodology, P.B. and L.A.; software, P.B.; validation, P.B., C.R. and L.A.; formal analysis, P.S., C.G., N.C., L.A.,G.M. and P.B.; investigation, P.S., C.G., N.C., L.A.,G.M. and P.B.; resources, A.V. and L.A.; data curation, P.B. and L.A.; writing—original draft preparation, P.B.; writing—review and editing, P.B.; visualization, P.B.; supervision, P.B.; project administration, P.B.; funding acquisition, N/A. All authors have read and agreed to the published version of the manuscript." Please turn to the CRediT taxonomy for the term explanation. Authorship must be limited to those who have contributed substantially to the work reported.

Funding: This research received no external funding.

Data Availability Statement: The data presented in this study are available in article.

Acknowledgments: The authors wish thanking Erwan Etienne for his help for several aspects of samples praparation.

Conflicts of Interest: The authors declare no conflict of interest.

References

1. Sims, C.T.; Hagel, W.C. *The Superalloys*; Wiley-Interscience, New York, U.S.A., 1972.
2. Donachie, M.S.; Donachie, S.J. *Superalloys: A Technical Guide*, 2nd ed.; ASM International: Materials Park, U.S.A., 2002.
3. Bracq, G.; Laurent-Brocq, M. et al. The fcc solid solution stability in the Co-Cr-Fe-Mn-Ni multi-component system. *Acta Materialia* **2017**, *128*, 327-336.
4. Liu, S. F.; Wu, Y. et al. Stacking fault energy of face-centered-cubic high entropy alloys. *Intermetallics* **2018**, *93*, 269-273.
5. Wei, D.; Li, X. et al. Novel Co-rich high performance twinning-induced plasticity (TWIP) and transformation-induced plasticity (TRIP) high-entropy alloys. *Scripta Materialia* **2019**, *165*, 39-43.
6. Choi, W.; Jung, S. et al. Design of new face-centered cubic high entropy alloys by thermodynamic calculation. *Metals and Materials International*, **2017**, *23(5)*, 839-847.
7. Kauffmann, A. ; Stueber, M. et al. Combinatorial exploration of the high entropy alloy system Co-Cr-Fe-Mn-Ni. *Surface and Coatings Technology* **2017**, *325*, 174-180.
8. Teramoto, T.; Yamada, K. et al. Monocrystalline elastic constants and their temperature dependences for equi-atomic Cr-Mn-Fe-Co-Ni high-entropy alloy with the face-centered cubic structure. *Journal of Alloys and Compounds* **2019**, 777, 1313-1318.
9. Berthod, P. As-Cast microstructures of high entropy alloys designed to be TaC-strengthened. *Journal of Metallic Material Research* **2022**, *5(2)*, 1-10. https://doi.org/10.30564/jmmr.v5i2.4685
10. Berthod, P. As–cast microstructures of HEA designed to be strengthened by HfC. *Journal of Engineering Sciences and Innovation* **2022**, *7(3)*, 305 - 314. https://jesi.astr.ro/wp-content/uploads/2022/10/3_Patrice-Berthod.pdf
11. Berthod, P. Strengthening against Creep at Elevated Temperature of HEA Alloys of the CoNiFeMnCr Type Using MC-Carbides. In Supplemental proceedings of the TMS 2023, San Diego, U.S.A., 19–23 March 2023.
12. Berthod, P. High Temperature Oxidation of CoNiFeMnCr High Entropy Alloys Reinforced by MC-Carbides. In Supplemental proceedings of the TMS 2023, San Diego, U.S.A., 19–23 March 2023.
13. Chenikha, N., Spaeter, P., Gay, C., Vernière, V., Berthod, P. Microstructures in as–cast condition of Medium Entropy Alloys designed to contain eutectic carbides TaC or HfC. *Journal of Engineering Sciences and Innovation*, submitted.
14. Berthod, P. Consequences of the additional presence of MC carbides on the behavior in oxidation at 1000°C of a cast Cantor high entropy alloy. *Materials and Corrosion* **202**3, 1-12. DOI: 10.1002/maco.202213721
15. Berthod, P. Kinetics of High Temperature Oxidation and Chromia Volatilization for a Binary Ni–Cr Alloy. *Oxidation of Metals* **2005**, 64(3/4), 235-252.